JOURNAL OF GEOPHYSICAL RESEARCH, VOL. 115, E03004, doi:10.1029/2009JE003464, 2010

Anticipated electrical environment within permanently shadowed lunar craters

W. M. Farrell,[1,2] T. J. Stubbs,[1,2,3] J. S. Halekas,[2,4] R. M. Killen,[1,2] G. T. Delory,[2,4] M. R. Collier,[1,2] and R. R. Vondrak[1,2]

Received 6 July 2009; revised 30 September 2009; accepted 20 October 2009; published 24 March 2010.

[1] Shadowed locations near the lunar poles are almost certainly electrically complex regions. At these locations near the terminator, the local solar wind flows nearly tangential to the surface and interacts with large-scale topographic features such as mountains and deep large craters. In this work, we study the solar wind orographic effects from topographic obstructions along a rough lunar surface. On the leeward side of large obstructions, plasma voids are formed in the solar wind because of the absorption of plasma on the upstream surface of these obstacles. Solar wind plasma expands into such voids, producing an ambipolar potential that diverts ion flow into the void region. A surface potential is established on these leeward surfaces in order to balance the currents from the expansion-limited electron and ion populations. We find that there are regions near the leeward wall of the craters and leeward mountain faces where solar wind ions cannot access the surface, leaving an electron-rich plasma previously identified as an "electron cloud." In this case, some new current is required to complete the closure for current balance at the surface, and we propose herein that lofted negatively charged dust is one possible (nonunique) compensating current source. Given models for both ambipolar and surface plasma processes, we consider the electrical environment around the large topographic features of the south pole (including Shoemaker crater and the highly varied terrain near Nobile crater), as derived from Goldstone radar data. We also apply our model to moving and stationary objects of differing compositions located on the surface and consider the impact of the deflected ion flow on possible hydrogen resources within the craters.

Citation: Farrell, W. M., T. J. Stubbs, J. S. Halekas, R. M. Killen, G. T. Delory, M. R. Collier, and R. R. Vondrak (2010), Anticipated electrical environment within permanently shadowed lunar craters, *J. Geophys. Res.*, *115*, E03004, doi:10.1029/2009JE003464.

1. Introduction

[2] The permanently shadowed lunar craters have a very complex environment. These locations are without direct sunlight and thus are very cold. The presence of low-temperature cold traps located just adjacent to sunlit regions allows for the collection of migrating volatiles as they pass into darkness, including the distinct possibility of trapping of water and other hydrogen-based compounds [see *Vondrak and Crider*, 2003, and references therein]. We suggest here that the polar environment is not only thermally and chemically complex, but also electrically complex with the development of a plasma miniwake, large surface potentials, inward-deflected ion flow and possible dust transport within the permanently shadowed craters (PSCs). As we describe, the electrical complexity may have a direct effect on the cold trap atom collection process.

[3] The fundamental process described herein is the expansion of solar wind plasma into any polar crater. The situation is illustrated in Figure 1. At the poles, the solar wind flows nearly horizontal to the surface and is significantly influenced by local topography. Specifically, for any large mountain or deep crater, solar wind flow will be altered (a solar wind orographic effect) whereby the solar wind plasma is absorbed on the upstream side of the obstacle and expands into the void formed downstream of the obstructing object [*Farrell et al.*, 2007]. In essence, a miniwake (i.e., miniature plasma wake as opposed to the global-scale wake that forms many lunar radii downstream of the moon) is formed on the leeward side of such obstructions.

[4] Plasma wakes/expansion regions are themselves complicated [*Crow et al.*, 1975; *Samir et al.*, 1983; *Singh et al.*, 1989; *Halekas et al.*, 2005]. Immediately behind the

[1]NASA Goddard Space Flight Center, Greenbelt, Maryland, USA.
[2]NASA Lunar Science Institute, NASA Ames Research Center, Moffett Field, California, USA.
[3]Goddard Earth Sciences and Technology Center, University of Maryland Baltimore County, Baltimore, Maryland, USA.
[4]Space Sciences Laboratory, University of California, Berkeley, California, USA.

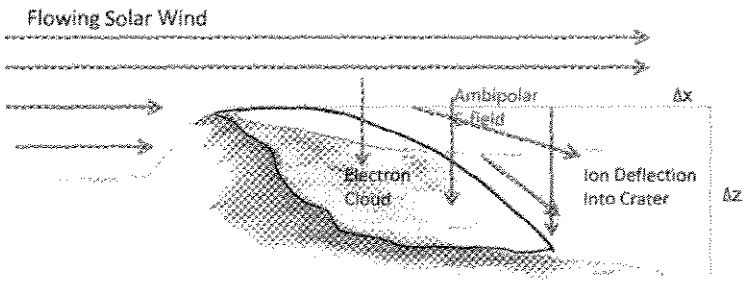

Figure 1. An illustration of the solar wind orographic effect over lunar polar craters. While the solar wind flow is initially horizontal, ambipolar electric fields draw ions into shadowed/solar wind obstructed cratered regions. Thus, ion trajectories are deflected into regions that would be considered "ion-free." Note the presence of an electron-rich region just leeward of the obstructed flow (called the electron cloud region) where electrons migrate into the void faster than the ions. In a steady state situation, the ions may never fully catch up to the electrons in these regions.

obstructing object, a plasma void is established. Thermal electrons at the edge of the void (along the flank of this void) expand into the region ahead of more massive ions because of their higher thermal velocity. Because of this charge separation, an ambipolar electric field (see Figure 1) develops across the wake flank to retard the electron flow and accelerate ions into the crater-generated void. As illustrated in Figure 1, originally horizontally flowing ions will be driven into the crater/void via the diverting force of the ambipolar E field. The ions tend to form beams that have a progressive increase in energy to many times the ion sound speed, C_s [*Crow et al.*, 1975]. As an analogous example, such ion beams are commonly detected near the wake flank of the space shuttle [*Singh et al.*, 1989] and were in fact detected by the Wind spacecraft in the large wake/void created antisunward of the Moon, at a distance of ~7 R_L [*Ogilvie et al.*, 1996].

[5] There are two views of the ion response in the void. *Samir et al.* [1983] presented a self-similar model where the expanding plasma remains neutral, i.e., where ions catch up with electrons to maintain quasi-neutrality ($n_e = n_i$) everywhere downstream of the obstruction. There is thus charge balance in the ambipolar region. However, if the quasi-neutral assumption is relaxed, it is found that directly behind the object, the ions never fully catch up, leaving an "electron cloud" in the wake region [*Crow et al.*, 1975], as illustrated in Figure 1. Particle-in-cell (PIC) plasma codes of the plasma expansion process also show this electron-rich region [*Farrell et al.*, 2008a] with the "cloud" really containing energetic electrons from the tail of the solar wind electron energy distribution. Compared to the solar wind plasma, the electrons in the cloud are velocity-filtered solar wind electrons of lower density and in the form of a beam at 2–3 times the solar wind electron thermal speed, v_{te}. As indicated in the analytical model of *Crow et al.* [1975] and PIC plasma codes [*Farrell et al.*, 2008a], the ambipolar E field reaches a maximum value at the inward limiting edge of the ion expansion (called the "ion front") [see *Crow et al.*, 1975, Figure 2]. The ambipolar potential is smoothly varying throughout the expansion region.

[6] While the difference between the charge neutral [*Samir et al.*, 1983] and nonneutral [*Crow et al.*, 1975] ambipolar models may appear to be an esoteric academic distinction, in reality the model perspective is critical in determining the surface potential at the bottom of lunar polar craters and behind polar mountains. Specifically, the local surface potential is defined by the current balance of all species reaching the surface. In shadowed/wake regions, there are typically three components that primarily define current balance: That from the solar wind electrons, solar wind ions, and secondary electrons emitted from the surface in response to the incoming plasma electrons. In this case, the shadowed surface potential, φ_s, assuming a Maxwellian distribution for electrons and ions, a thin sheath, and planar geometry is [*Manka*, 1973]:

$$e\varphi_s \sim -kT_e \ln(J_e(1-\delta_{eff})/J_i) \quad (1)$$

where T_e is the electron temperature, $J_{e,i}$ are the electron and ion current density, respectively, and δ_{eff} is the effective coefficient for secondary electron emission from the lunar surface that has a value near 0.2–0.8 for an electron temperature of ~10 eV [*Halekas et al.*, 2002, 2009a]. The electron and ion currents are those located at a point just above the Debye sheath along the crater walls and floor.

[7] Herein lies the dilemma: If the *Samir et al.* [1983] charge neutral model accurately represents ambipolar processes, electron and ion densities are forced to be equal everywhere downstream of the obstacle. The densities become $n_e \sim n_i \sim n_{eo} \exp(e\varphi_A/kT_e)$ where φ_A is the ambipolar potential drop (which is a negative potential). By forcing electron and ion concentrations to remain equal, one can always obtain current balance between inflowing solar wind electrons, surface emitted secondary electrons, and solar wind ions, allowing the surface potential to be easily quantified via equation (1). In essence, the ions will veer from their original horizontal flow and propagate into the crater in cadence with the thermally expanding electrons. On the other hand, if the *Crow et al.* [1975] nonneutral ambipolar model more accurately characterizes wake expansion, there will be regions just behind the obstacle that are immersed in the electron cloud, with no solar wind ions present (see Figure 1). An electron-rich plasma will then exist at locations where the well-directed ion flow cannot reach the surface, especially at locations in the crater where the local

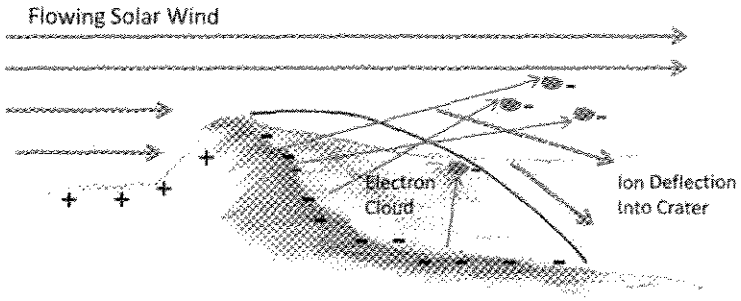

Figure 2. The strong negative surface charging within the electron cloud region may be remediated by lofted negatively charged dust that acts as a possible current of last resort to keep the potentials from becoming extremely large.

surface normal points away from the flow (i.e., the face of the surface is not incident in any way with the flow). As is clear from equation (1), absent other current sources, the surface potential at such locations goes to negative infinity because current balance closure is never achieved. Without the ions or some other positive current to the surface to balance the electron current, the surface charging goes as $dQ/dt = J_e (1 - \delta_{eff}) \exp(e\varphi_s/kT_e) < 0$ for all times: the surface perpetually charges negative.

[8] Obviously, this is unrealistic. If the potentials become too large, some other near-surface process creates a "breakdown" current to provide the required current balance. The quantity J_i in equation (1) is thus replaced by this other current. One possibility is that the secondary electron production increases as potentials get progressively larger (δ_{eff} approaches unity under larger potentials). This secondary production increase may be especially relevant to kappa electron distributions, where Te increases progressively with distance from the wake flank [*Halekas et al.*, 2005] thereby creating greater secondary production (which varies as T_e). In the most extreme case, this secondary emission might even take the form of "field emission" from surface irregularities. It may be argued that a large surface potential at the crater floor will draw in ions that are originally flowing at larger distances from the crater floor. However, for a crater surface located 10 Debye lengths from the ion flow (~150 m), the surface potential will have to overcome a Debye shielding attenuation of nearly a factor of 10^6 and for 20 Debye lengths distance, a shielding attenuation of nearly a factor of 10^9. Only in locations close to the ion flow (within a few Debye lengths of the ion flow) will there be significant ion diversion to remediate the perpetually negative surface charging.

[9] However, another possible process that has received much discussion is lifted/lofted charged dust from the surface that may act as a natural current source to remediate large potential development. Specifically, assuming an electron rich plasma reaches the leeward wall of the crater, the surface and loose dust will be charged with similar polarities (both negative). If surface potentials become large and negative, then the local E fields may become large enough to loft the like-charged dust [*Stubbs et al.*, 2006]. This lofted dust current J_D (consisting of upward-moving negative charge) may act "as a current of last resort" in place of the inflowing positive ions, J_i, in the electron cloud region. In this work, we will attempt to quantify such a dust current and incorporate it into surface charging models. As we show, the dust currents should be emitted from the leeward surfaces of polar obstacles (mountains, crater walls) where inflowing ions are not directly incident on the surface, creating an antisunward dust flow that may be reminiscent of the Apollo 17 Lunar Ejecta and Meteorite (LEAM) observations in the Taurus-Littrow valley [*Berg et al.*, 1976; *Farrell et al.*, 2007]. The situation is illustrated in Figure 2.

[10] In this work, we will use topographic relief of the lunar south polar region provided by Goldstone radar observations [*Margot et al.*, 1999] to quantify the obstacle dimensions that creates the solar wind orographic effect. We assume that the solar wind plasma has a near-horizontal flow overtop the region, and we then derive values of the two potentials (ambipolar and surface potential) that affect both electron and ion migration into permanently shadowed craters (PSCs) like Shoemaker and Shackleton. We will ultimately display a potential map and indicate regions where dust lofting and object dust cling may be the greatest.

2. Topography of the South Polar Region

[11] Figure 3a shows the Goldstone 3.5 cm (8.6 GHz) solar system radar measurements from the south polar region of the Moon [*Margot et al.*, 1999]. The delay in return echoes allow a measurement of relative altitude and thus provides a topographic map of the region with 600 m resolution. The data are available from the Planetary Data System and measurement details are further described by *Margot et al.* [1999].

[12] As indicated in Figure 3a, there is substantial relief in the region. The varied topography provides an optimal case for developing a solar wind orographic/plasma expansion model. To the northeast, near 85S,45E, there are mountains that extend to nearly 6 km in height but the terrain also appears to be marked by impacts like Nobile crater that create abrupt changes in the local relief. Shackleton crater is clearly evident in the radar measurement near 89.7°S, 100° E. Unfortunately, the radar signal did not map the entire floor of this crater. Hence, for crater modeling we use the larger Shoemaker crater located at about 88°S, 45°E which has a set of clear and distinct echoes from the southern portion of the floor. Figure 3b shows a topographic profile across the southern portion of Shoemaker crater, with the

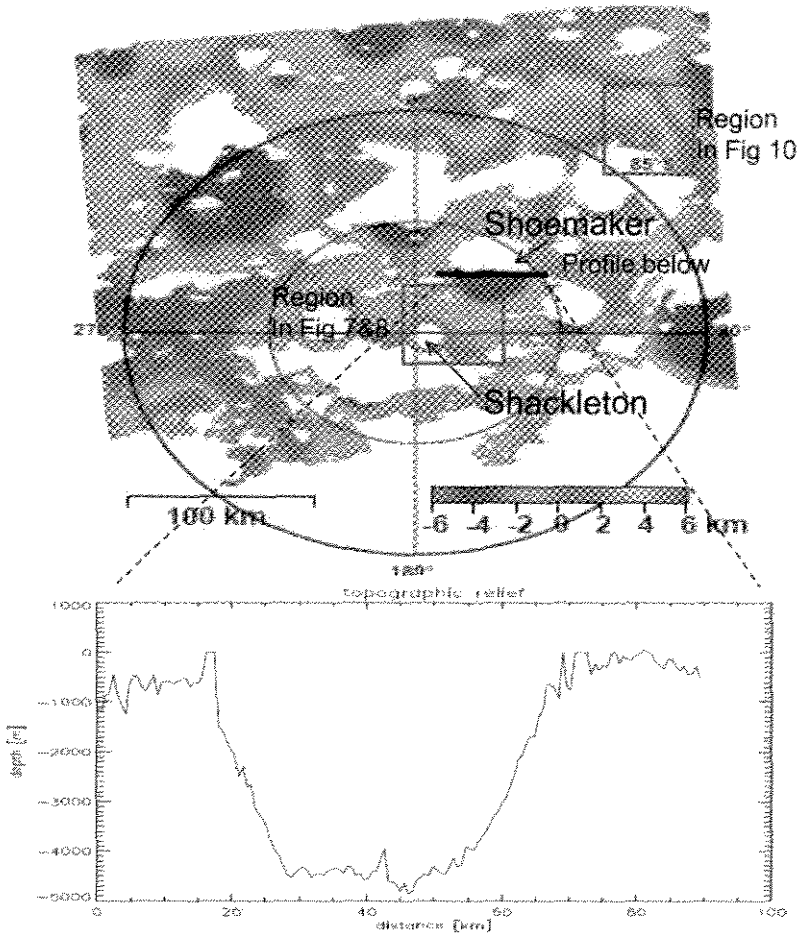

Figure 3. A topographic map of the south polar region obtained from the Goldstone 8.6 GHz radar system. A profile of the topography across Shoemaker crater is also displayed, and this profile is our primary test case used in the study. Regions used to obtain surface potential maps in Figures 7, 8, and 10 are indicated by blue rectangles.

crater floor at 4800 m depth. This particular profile is used as our standard test case. We also indicate the locations of our regional analysis presented in Figures 7, 8, and 10.

[13] We later apply the plasma expansion/surface potential algorithm to larger regions, which will prove to be very revealing. In order to run such regional models, the determination of the ambipolar potential and surface potential behind polar mountains and within polar craters has to be streamlined. We apply the analytical model of *Crow et al.* [1975] to map the ambipolar potential and we perform a very simple surface potential calculation to achieve the results at large scale. The process is described further below.

3. Ambipolar Potential

[14] Any charged particle reaching the surface downstream from an obstruction has to pass through two negative potentials: one associated with the expansion process itself (the ambipolar potential) and a second near-surface sheath potential defined by local current balance at the surface. Any electron has to have enough energy to pass through both potentials, and as such, only the most energetic electrons at the tail of the solar wind electron energy distribution possess the energy required to extend deep behind the leeward sides of obstructions.

[15] As illustrated in Figure 1, the ambipolar potential extends from the flank/edge into the central region of the void. *Halekas et al.* [2005] measured the large-scale electron density and ambipolar potential across the global lunar wake at low altitudes (20–115 km) using >6000 passages by the Lunar Prospector (LP) spacecraft. They clearly mapped out the reduced density and potential structure behind the Moon and found that the expansion could be fit to a modified self-similar model like that of *Samir et al.* [1983]. The model of *Crow et al.* [1975] and *Samir et al.* [1983] have similar electron density and ambipolar potential profiles as the plasma expands into the void. Without ion measurements, LP could not determine uniquely if the expansion is charge balanced or unbalanced. However, simulations of the lunar expansion [*Farrell et al.*, 1998; *Birch and Chapman*, 2001a, 2001b] suggest that there is an imbalance. Both cases with be considered herein.

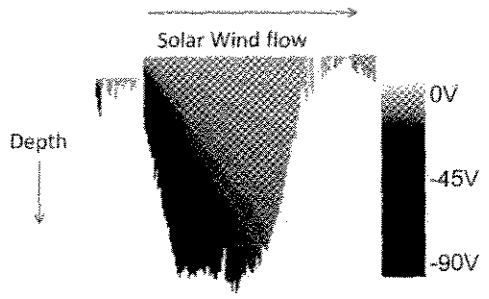

Figure 4. The strength of the ambipolar potential within Shoemaker crater for a westward horizontally flowing solar wind. Note that the largest ambipolar potentials exist just leeward of the obstacle (i.e., crater's west wall). The initial solar wind conditions that define the properties of the wake expansion are n_{eo} = 5/cm^3, 10 eV temperature, and Vsw ~ 400 km/s, implying a 15 m Debye length and ω_{pi} = 3000/s and a 0° elevation angle with the solar wind coming out of the west. Table 1 provides more plasma flow details at specific points along the crater floor for this particular simulation run.

[16] Both *Crow et al.* [1975] and recent simulations [*Farrell et al.*, 2008a] map out the ambipolar potential (E field) behind an obstacle as a function of distance behind the obstacle and depth into the void. Both results are comparable. *Crow et al.* [1975] provides the calculations in normalized units that can be easily converted to a general relationship assuming a time stationary structure. Fitting to those values, we find that the ambipolar potential varies approximately as

$$e\varphi_A/kT_e = -1.08\left(z'/t'\right) - 1 \tag{2}$$

where the plasma is expanding into distance z' defined by *Crow et al.* [1975] as the normalized depth into a crater, $\Delta z/\lambda_D$ and t' is the normalized time of the expansion, $\omega_{pi}t$. We note that equation (2) is also nearly identical to the expansion potential defined by *Samir et al.* [1983] and thus the two formalisms (charge neutral and nonneutral) provide nearly identical downstream potential structures. The variable Δz is the vertical distance from the wake flank into the void. At $t' = 0$, the plasma void is formed and the plasma discontinuity is in the form of a perfect step function located at $z' = 0$ (exactly along the wake flank). As time evolves, the plasma expands along z', moving Δz into the void. For a time stationary wake, the time t' corresponds to a specific distance that a solar wind plasma fluid element has convected downstream from the obstacle, $t' = \Delta x\omega_{pi}/V_{sw}$ with this downstream distance, Δx, being the horizontal distance from the obstacle edge (see Figure 1). As such, the ambipolar potential inside a crater for nominal solar wind conditions (n_{eo} = 5/cm^3, T ~ 10 eV, 15 m Debye length, Vsw ~ 400 km/s, and ω_{pi} = 3000/s) is

$$e\varphi_A/kT_e = -9.7(\Delta z/\Delta x) - 1 \tag{3}$$

For example, consider solar wind flowing horizontally at the terminator or polar region over an obstruction of 1 km in height. At distance of 500 m behind the obstacle on the leeward side of the obstruction, the value of $\Delta z/\Delta$ x is 2 making the local ambipolar potential from equation (3) at $\varphi_A \sim -20\ kT_e/e$ or ~−200 V relative to the solar wind plasma potential. The local electron density is

$$n_e/n_{eo} = \exp(e\varphi_A/kT_e) \tag{4}$$

and is reduced by 10^9 compared to solar wind values. At a distance of 1 km behind the obstacle, the local electron density is reduced by only 10^5 compared to solar wind values, indicating that the solar wind plasma is further filled in at this distance.

[17] Figure 4 shows the ambipolar potential within Shoemaker crater (i.e., our test profile), assuming the solar wind flow is horizontal and out of the west. The initial solar wind conditions that define the properties of the wake expansion are n_{eo} = 5/cm^3, 10 eV temperature, and V_{sw} ~ 400 km/s, implying a 15 m Debye length and ω_{pi} = 3000/s. This case was run with the solar wind at a 0° elevation angle (horizontal flow) relative to the overall surface. The starting point for the expansion into the void is the relative maximum in the surface located at the x = 18.6 km. As indicated by the dark regions, the ambipolar potential is largest along the leeward facing wall. Figure 5 shows the ambipolar potential values at the floor of the crater (topographic profile also included). Note that at the leeward edge of the crater (Figure 5, left), the near-surface ambipolar potentials can drop as low as −90 V. This ambipolar potential acts to retard thermal electron flow and force ions to catch up to the faster electrons.

4. Surface Potential

[18] The surface potential along the crater floor is defined by the currents that reach the surface after passing through the ambipolar potential. In essence, the ambipolar potential "filters" the solar wind reaching the surface. A second near-surface potential (the sheath potential) then forms to create current balance at the surface. We now address the formation of this second potential.

[19] To define the ambipolar currents that reach any point within a PSC, we apply a *Samir et al.* [1983] expansion of Maxwellian plasma with $n_e = n_i = n_{eo}\exp(e\varphi_A/kT_e)$, where n_{eo} is the density of the ambient free-flowing solar wind away from the obstacle and we initially assume a neutral plasma. The ion expansion velocity is $(\Delta z/t) + C_s$ where C_s is the ion sound speed ($=\lambda_D\omega_{pi}$) and as we demonstrate will have a specific flow angle at the surface, defined as θ_{flow}. *Samir et al.* [1983] and *Crow et al.* [1975] define the evolution of the wake by a time after the formation of the void, t. In an assumed time stationary flow, this time can be replaced by the $\Delta x/V_{sw}$, where Δx is the horizontal distance from the obstacle edge (see Figure 1) and V_{sw} is the downstream ion flow velocity [*Farrell et al.*, 1998]. The near-surface plasma currents in the ambipolar region for near-horizontal solar wind flow are thus described as

$$J_e \sim n_{eo}\, e\, v_{te} \exp(e\varphi_A/kT_e)(1 - \delta_{eff}) \tag{5a}$$

$$J_{iz} \sim -n_{eo}\, e(((\Delta z/\Delta x)V_{sw} + C_s) + V_{sw}\mathrm{Sin}(\theta_{sw}))\exp(e\varphi_A/kT_e) \tag{5b}$$

$$J_{ix} \sim n_{eo}\, e\, V_{sw}\mathrm{Cos}\,(\theta_{sw})\exp(e\varphi_A/kT_e) \tag{5c}$$

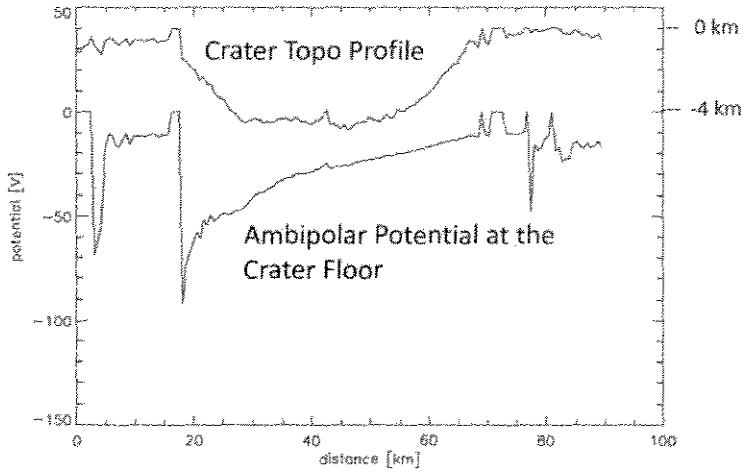

Figure 5. The ambipolar potential along the crater floor for the case run in Figure 4 and Table 1.

where $\varphi_A = \varphi_A(\Delta x, \Delta z)$ is the ambipolar potential calculated at the floor of the crater (shown Figure 5) that has a gradient in both x and z. As a consequence, the ambipolar E field also is a function of both variables. Variable v_{te} is the electron thermal velocity which varies as $T_e^{1/2}$. The angle θ_{sw} is the initial elevation angle of the solar wind relative to the x direction, which is assumed to remain relatively small for nominal solar wind near the south pole. We assume the electron current incident at the surface releases secondary electrons with an efficiency δ_{eff} between 0.2 and 0.8 [*Halekas et al.*, 2002, 2009a]. The geometry defining Δz and Δx is illustrated in Figure 1.

[20] The thermal electrons are assumed to be quasi-isotropic. However, the ions form a well-defined and directed beam that develops a vertically downward component, v_z, at the expansion speed of $(\Delta z/\Delta x)\, V_{sw} + C_s$. Now consider a solar wind flow that initially is oriented along the x direction ($\theta_{sw} = 0°$). As the plasma propagates downstream from the obstacle, plasma is drawn into the void region, with a rarefaction wave propagating upward into the solar wind and plasma expansion downward into the ambipolar region [e.g., *Samir et al.*, 1983, Figure 11]. In this ambipolar expansion region, the ions flow inward with a perturbed deflection angle, $\theta_{flow} = \arctan(J_{iz}/J_{ix}) \sim \arctan((\Delta z/\Delta x) + (C_s/V_{sw}))$. Note that for distances close to the obstructing source, $\Delta z/\Delta x >> 1$, the ion flow diverts substantially from its initially horizontal direction. For example, the depth in the z direction, Δz, in Shoemaker crater is ~5 km at the floor. At a distance of 5 km from the obstruction edge, the ion flow diverts into the crater at an angle of ~30° due to the strong ambipolar fields. In the middle of the crater at 50 km, the deflection angle is closer to 10° and for large distances from the obstruction edge, the angle reaches an asymptotic value near 6° from the horizontal (i.e., the ion sonic Mach cone angle).

[21] As evident in the equations, the electron are repelled by the negative ambipolar potential, and are limited to reaching the surface by a repulsive force varying as exp $(e\varphi_A/kT_e)$ (factor in equation (5a)). In contrast, the cold ions are accelerated by the wake potential into the crater. The surface potential is then calculated assuming current balance at the surface in a thin sheath planar geometry:

$$J_e \exp(e\varphi_s/kT_e) - |J_i|\mathrm{Sin}(\theta_{flow} - \theta_{topo}) = 0 \qquad (6)$$

where J_e and J_i are from equation (5) and θ_{topo} is the elevation angle of the local surface.

[22] Table 1 lists the current densities and surface potential as a function of variable x – the location along the crater floor in Figure 5. Note that J_i can drop below 10^{-10} A/m^2 at the bottom of the crater (near the leeward edge). As also

Table 1. Electrical Environment Characteristics as a Function of Location Along Crater Floor[a]

	x (km)				
	18.6	20	30	40	50
J_i (A/m^2)	4.6×10^{-11}	7.7×10^{-11}	1.0×10^{-9}	5.4×10^{-10}	6.7×10^{-9}
φ_A (V)	−74	−63	−41	−29	−23
φ_s (V)	−16	−22	−18	−37	−18
φ_o[b] (V)	+6; +45	+6; +45	+6; +45	+6; +45	+6; +45
1/e Dissipation time (s)	60	40	2.8	5.6	0.4

[a]The variable x is the horizontal distance across Shoemaker crater shown in Figure 3. The initial solar wind conditions that define the properties of the wake expansion are n_{sw} = 5/cm^3, 10 eV temperature, Vsw ~ 400 km/s, and these make a 15 m Debye length and ω_{pi} = 3000/s, and a 0° elevation angle of the solar wind coming out of the west, identical conditions to those run for Figures 4, 6, and 7a. The crater edge is x ~ 18.6 km location.

[b]Here +6 V for object with secondary emission δ_{eff} ~ 0.5 and +45 V for object with secondary emission δ_{eff} ~ 0.99.

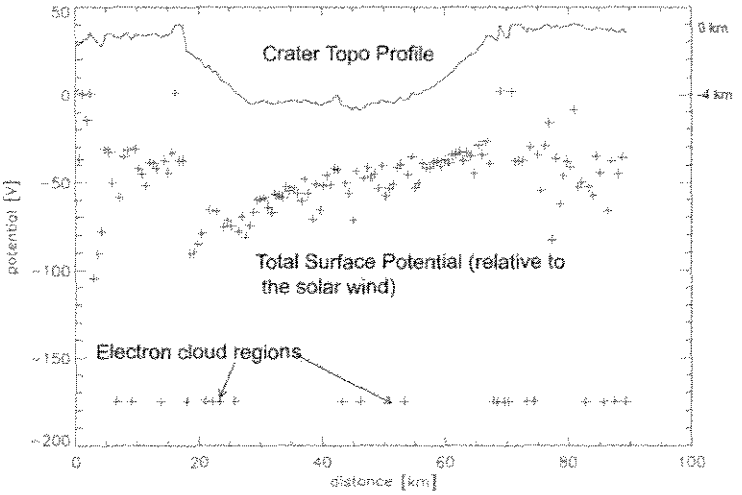

Figure 6. The total potential (surface + ambipolar) relative to the solar wind along the crater floor for conditions applied to Figure 4 and Table 1. The values near −180 V are associated with crater floor locations where ion flow is inaccessible; the locations are within the electron cloud. We assume upward dust currents thus provide closure for current balance.

indicated in Table 1, the overall potential is the largest at the leeward edge of the crater: the two electron retarding potentials ($\varphi_A + \varphi_s$) gives the total potential at the surface relative to the solar wind close to ~−90 V near x = 18 km. Thus, a solar wind electron has to be energetic enough to pass through both negative potentials φ_A and φ_s to reach the surface – which greatly limits the local environmental currents at the floor of the PSC. The density of electrons is thus $n_e \sim n_{eo} \exp(e(\varphi_A + \varphi_s)/kT_e) \sim 5 \times 10^{-4}/cm^3$: a nearly 10,000 to 1 electron rejection from the original solar wind electron flow overtop the crater assuming a Maxwellian plasma distribution.

[23] While the electrons thermally advance into the crater at the thermal speed, the ions have a very specific and directed flow. As a consequence, there are distinct locations along the crater floor where ion currents simply do not flow onto the surface and the regions are thus immersed in the *Crow et al.* [1975] electron cloud. Figure 6 indicates that locations like the leeward crater wall and local maximum within the crater itself (like near the x = 45 km location) are possible topography features where ion flow may become compromised. Unfortunately, current balance at these surface locations is never reached: $dQ/dt = J_e \exp(e\varphi_s/kT_e) < 0$ and the simple solutions are a continuous accumulation of negative charge until the potential goes to negative infinity. This is physically unrealistic and thus we infer the presence of some other "current of last resort" that gets established to provide closure for current balance.

[24] An obvious (but nonunique) choice of currents is that from dust grains repulsed from the strong negatively charged surface immersed in the electron cloud. The LEAM impact detector operating at the Apollo 17 Taurus-Littrow valley landing site measured greatly increased dust activity at lunar terminator crossings which have been interpreted as dust impacts at tens of m/s that were suggested to be accelerated by terminator E fields [*Berg et al.*, 1976; *Berg and Perkins*, 1979]. The flow of these grains is greatest toward the night side directions, implying that the solar wind leeward edges of the surrounding mountains became strongly negatively charged (see Figure 2). LEAM detected an impact about every two minutes and to be detected the grain had to contain about 10^{-12} C of charge [*Berg et al.*, 1976]. LEAM was not initially designed to detect these slower moving grains and there is some ambiguity in the determination due to the dissipation time of the LEAM pulse height capacitor sensor [*Berg and Perkins*, 1979]. As such, the detection flux appears to be correct but the detailed physical properties of the grains (speed and charge) remains of some debate.

[25] If we assume the quoted *Berg et al.* [1976] results, then the current density for these grains is $J_{Do} \sim A^{-1} Q_d/\tau \sim 10^{-14}$ A/m^2, where A is assumed to be the size of the detecting system (0.01 m^2), Q_d is 10^{-12} C and τ is the dust incidence time of ~100 s. We now incorporate this dust current in regions where ions are not directly incident. We might also suggest that there is some dependency of released dust on surface potential ($J_D = J_{Do} \exp(\varphi/\varphi_f)$) but to assume some value of scaling potential, φ_f, would make the situation even more contrived. Hence, we leave a more advanced synopsis of the dust reaction for future work.

[26] Figure 6 shows the total (surface and ambipolar) potentials relative to the solar wind along the topographic profile of Shoemaker crater. We assume the solar wind passing over the top of the crater has an initial $n_{eo} = 5/cm^3$, T = 10 eV, $V_{sw} \sim 400$ km/s, $\gamma_{eff} \sim 0.3$ and westward flow with an elevation angle, $\theta_{sw} = 0°$ (initial all horizontal flow). Note that the surface becomes strongly negative along the leeward edge of the crater, dropping to values near −100 V. Each of these solutions (values >−120 V) has ions present at the surface location, thus allowing current balance and a unique solution for the surface potential. The local topographic gradient angle and ion flow angle are included in the solution, and account for the large variation in surface

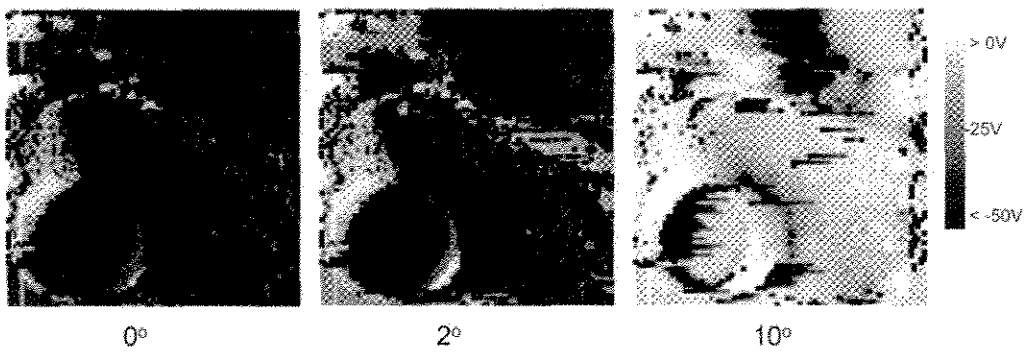

Figure 7. A 54 km × 54 km regional view of the surface potential at Shackleton crater (bottom left) and the southern portion of Shoemaker crater (top right). The westward flowing solar wind elevation angle and solar illumination angle are 0°, 2°, and 10°, respectively. The 10° case is provided as an illustration of extreme angles, but solar illumination at such angles never really occurs near the south lunar polar regions presented. White regions represent total potentials at the surface of >0 V and dark regions are <−50 V. Note that strong negative potentials exist within the shadowed craters, especially along the western/leeward faces.

potentials along the crater floor. At the crater floor, local surfaces that have normals oriented into the ion flow will have a decreasing negative potential (larger J_i), while surfaces with normals directed away from the ion flow will have larger negative potentials (smaller J_i).

[27] However, there are clearly locations where the ions do not flow directly to the surface. One such location is near the bottom of the leeward-facing crater wall (x = 18 to 20 km in Figure 6). In these cases, we assume upward negative dust currents replace downward ion currents, making the total potential drop near −180 V (the crosses located near the bottom of Figure 6). In this electron cloud region, the total potential at the surface relative to the solar wind is $e\varphi_s = e\varphi_A(z) - kT_e \ln (J_e (1 - \delta_{eff})/J_{Do})$ and is dependent on the assumed dust current (or some other breakdown current). Since $J_e \sim n_{eo}\, e\, v_{te} \exp(e\varphi_A/kT_e)$, one then finds that $e\varphi_s \sim -kT_e \ln(n_{eo} e\, v_{te}(1 - \delta_{eff})/J_{Do})$ which is quasi constant. Obviously, this J_{Do} current of last resort applied herein is not unique, and we leave open the possibility of some other breakdown current that has yet to be identified.

5. Regional Views

[28] The total potential at the surface can be calculated across an entire region, taking the steps above and repeating them for each topographic structure. Figure 7 shows a 54 km × 54 km region containing Shackleton crater and the southern rim of Shoemaker crater (see boxed area indicated in Figure 3). We note that radar signals did not extend into the floor of the smaller Shackleton crater and all elevations were set to a constant value of 0 km relative to the mean lunar radius. This floor value is still well below the crater rim and gives rise to ambipolar expansion effects. In this process, relative maxima were identified. On the forward, sunlit side of the structure, both solar wind and photoemission currents dominate and the surface potential is easily derived from current balance. For the sake of demonstration we have aligned the solar illumination and solar wind directions. However, the code can consider separate radiation and particle elevation angles. On the leeward side of the structure, the location of the surface relative to the obstruction maximum height is determined, and both ambipolar and surface potentials are derived using equations (3), (5), and (6).

[29] Figure 7 shows the total surface potential relative to the solar wind ($\varphi_A + \varphi_s$) under a solar illumination and solar wind elevation angle θ_{sw} of 0° (Figure 7, left), 2° (Figure 7, middle), and 10° (Figure 7, right) above the western horizon. We note that the case for 10° is in fact fictitious and that solar illumination never extends to that elevation above the horizon at this polar location. However, the case is used to demonstrate the effect of sun rise on the region and would be applicable for a similar crater at midlatitudes crossing the terminator. The initial solar wind conditions that define the properties of the wake expansion are n_{eo} = 5/cm^3, 10 eV temperature, δ_{eff} = 0.3, Vsw ~ 400 km/s, and these correspond to a 15 m Debye length and ω_{pi} = 3000/s for use in equations (3)–(6). The dark regions correspond to potentials at values below −50 V. Note that negative potentials are located on the leeward sides of orographic structures and inside the leeward/western faces of craters. At 10° elevation angle, the region has a larger portion of the surface exposed to direct solar wind and solar radiative flux, and hence the area of negative potential is correspondingly reduced.

[30] Figure 8 shows the same region calculated with $\theta = 2°$ but for a warmer plasma consistent with that from a solar coronal mass ejection (CME). Specifically, a CME consists of an explosive release of driver gas from the sun. As the CME driver gas propagates toward the Earth at supersonic speeds, a bow shock and plasma sheath (similar in nature to a magnetosheath) develops forward of the CME driver gas. The ambient low energy plasma in the sheath region consists of densities nearly 4 times the ambient solar wind, warmer plasma at many 10 s of eV, and faster flowing plasma at 600–800 km/s. For Figure 8, we run the case for ambient densities near 20 el/cm^3, plasma temperatures of 40 eV, and flow speeds at 600 km/s. Since secondary emissions vary roughly as T_e in this regime, we also assume a higher surface secondary electron coefficient of $\delta_{eff} \sim 0.8$. Note

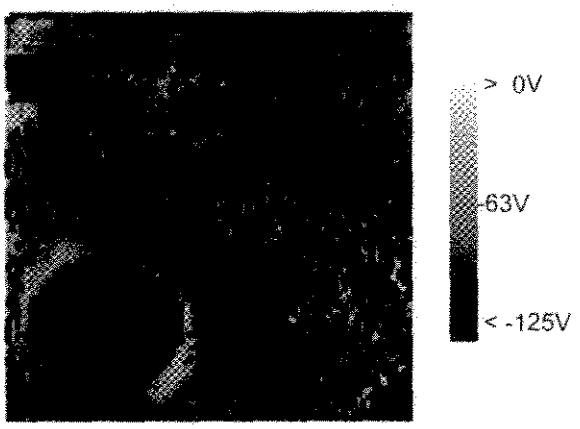

Figure 8. The same region as Figure 7 but now with solar wind conditions during a passing CME (n_{eo} = 20 el/cm^3, T ~ 40 eV, and Vsw ~ 600 km/s, solar wind elevation angle of 2°, and δ_{eff} ~ 0.8). Black regions now indicate surface potentials <−150 V.

that as the solar wind becomes warmer, the surface potentials behind obstructed regions become strongly negative. Figure 8 shows that most of the region has a surface potential below −125 V.

[31] Figure 9 shows a profile along the floor of Shoemaker crater during a passage of a CME. Figure 9 is analogous to Figure 6, only now the westward flowing solar wind is moving at 600 km/s, with a temperature of 40 eV and density of 20 el/cm^3. Note that the region of largest potential drop is located along the leeward flank of the crater, with surface potentials about 3 times greater during the CME sheath passage as compared to nominal solar wind conditions shown in Figure 6.

[32] We note that Figures 8 and 9 are associated with changes in the "cold" plasma during a solar storm/CME direct passage to the Moon. We do not consider herein the effect from solar energetic particles (SEP) events that are associated with a solar flare/CME formation. Such energetic particles propagating at relativistic speeds arrive at the Moon days before the CME driver gas and sheath modeled herein. These energetic particles also have the capability to create anomalous surface charging to large negative values, as has been reported by *Halekas et al.* [2007, 2009b]. *Halekas et al.*'s [2009b] recent modeling of the measured particle spectrum from low to high energies should enable the additional contribution of such high-energy currents from SEPs to be included in our model and this will be presented in future efforts. We only consider the cold plasma variations at this time, to focus on plasma expansion in crater-formed miniwakes.

[33] As another example, we include a regional view of the highlands located near 84°S, 40°E (Figure 10). These mountains extend 6 km in height but are modified by the impact basin associate with Nobile crater – giving rise to stark contrasts in topography. For the model, we assume the solar wind elevation angle is θsw = 1° above of the local horizon, flowing directly out of the east. The dark region represent locations where the surface potential is <55 V and light regions represent locations where the surface potential is >0 V. Note that the highlands do indeed act as orographic structures that create ambipolar fields and large, negative surface potentials within the crater regions.

6. Objects on the Crater Floor

[34] While the surface charges in an attempt to balance the upward and downward current flows, any object placed on the surface will become charged in these same environmental currents. However, because the object has a differing secondary electron character and sheath character (large compared to object size) the potential of the object, φ_{obj}, will differ from that of the surface. Specifically, the surface will charge to obtain current balance, and these local

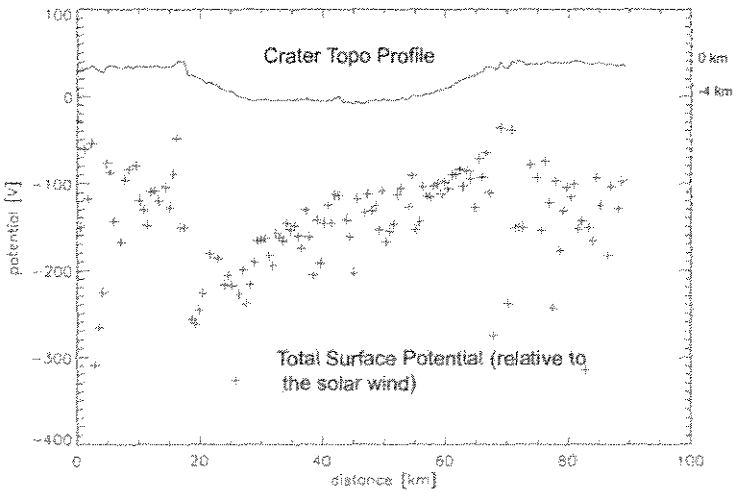

Figure 9. The same surface topographic region as Figure 6, now with similar storm conditions as Figure 8.

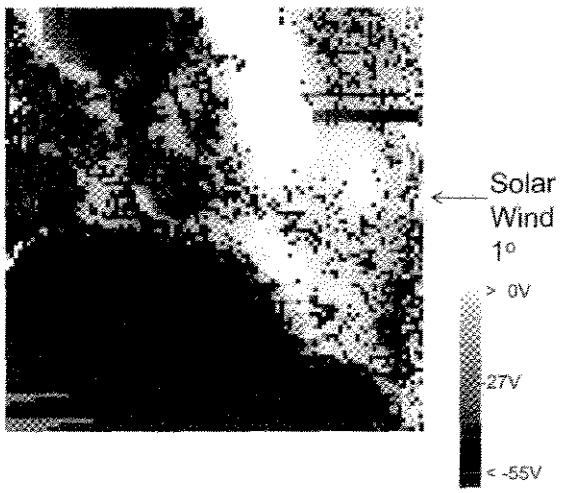

Figure 10. The potential in the 60 km × 60 km region at the edge of the highlands located at 84°S, 40°E. This region includes an abrupt topographic change defined by the northeast rim of Nobile crater. In this case, the solar wind is flowing out of the east at a 1° elevation angle, with $n_{eo} = 5/cm^3$, 10 eV temperature, Vsw ~ 400 km/s. Note that the dark regions are indicative of surface potentials <−55 V while white regions are potentials >0 V. The highland surfaces facing the sun/solar wind obtain positive potentials while the Nobile crater floor develops a strong negative potential.

environmental currents in the sheath that form along the crater floor are

$$J_{e-env} \sim n_{eo}\, e\, v_{te} \exp(e\varphi_T/kT_e)(1 - \delta_{eff}) \sim J_{i-env} \qquad (7)$$

where the total surface/solar wind potential drop is $\varphi_T = \varphi_s + \varphi_A$. To complete the calculation, we assume that the object is not located in the electron cloud and has direct access to the local ion beam. We also assume that the object can redistribute its charge quickly over its surface. Given these assumptions, the object is immersed in these environmental currents and will become charged as it attempts to balance the electron and ion flux incident at its surface. This static current balance at the object surface can be expressed as

$$J_{e-env}\left(1 - \delta_{eff}^{obj}\right) \exp\left(e\varphi_{obj}/kT_e\right) - J_{i-env} = 0 \qquad (8)$$

The ion current from the incident wake beams is defined as $J_{i-env}\,[1 - e\varphi_{obj}/mv^2]$ where v is the beam velocity. However, for a beam energy near 1 keV, $e\varphi_{obj}/mv^2 \ll 1$ and thus has a negligible contribution. The object's secondary electron emission is included in the factor δ_{eff}^{obj}. We assume the object is small compared to the local Debye sheath and thus the object is acted upon by the local currents at the crater floor. As indicated in equation (7), electron and ion currents are nearly equal at the surface as forced by the surface potential. If the object is larger than the sheath, then the environmental currents from the ambipolar region are directly incident (i.e., those described in equation (5)). These ambipolar currents are no longer balanced. We do not consider this case, but choose to leave the nomenclature for J_{e-env} and J_{i-env} in equation (8) for completeness even though they approximately cancel for this application. Table 1 indicates the object surface potential difference assuming two differing secondary electron emission characteristics: $\delta_{eff}^{obj} = 0.99$ and $\delta_{eff}^{obj} = 0.5$. We note that the more emissive object charges to a larger potential than the lunar surface. For poor secondary electron emitters, like many insulators, some concern has to be given to the redistribution of charge over the object. If that is slow, then the object may differentially charge based on access to the ion flow. A full 3D model of an object is not considered herein, but certainly worthy of consideration for future efforts.

[35] As an object (astronaut, rover) moves over the regolith, it is anticipated to collect charge via frictional/contact electrification effects between the object and regolith. This dynamic phenomenon is commonly called tribocharging. The charge exchange is associated with the differing contact potentials (which are related to the work function) between materials [*Desch and Cuzzi*, 2000]. Typically, if a metallic material comes in contact with an insulating material, the metal will gain a net charge negative while the insulator will obtain a net charge positive. The charge amount for smaller objects is a direct function of the triboelectric potential difference and related to size differences (relative capacitance) of the object.

[36] It was recently shown that an object on the lunar surface can be modeled via an equivalent circuit consisting primarily of a capacitor connected to both the free charge in the regolith and the plasma [*Farrell et al.*, 2008b]. As an object roves over the surface, it will become tribocharged. However, since the lunar regolith is a poor conductor, the object is most easily grounded via the conductive plasma. The electrical dissipation time to remove excess tribocharge is $\tau \sim (C\,kT/eJ_{env}A)$, where C is the object capacitance, J_{env} is the environmental current of opposite polarity to the object charge polarity (positively charged object draws in environmental electrons, negatively charged object draws in environmental ions), T is the temperature of the species drawn to the object, and A is the current-collecting area of the object.

[37] Within the very cold shadowed regions, the regolith conductivity is very low, ~10^{-14} S/m [*Carrier et al.*, 1991] and electrical dissipation into the regolith is very slow. However, as we demonstrate in Table 1, local plasma currents also become choked off behind obstacles due to the passing flow and both the ambipolar and surface potentials. As such, electrical dissipation times increase greatly.

[38] Because tribocharging is dynamic, the electrical system does not achieve current balance when tribocharging. Hence, a charging equation is solved:

$$C\, d\varphi_{obj}/dt = J_{e-env} A\left(1 - \delta_{eff}^{obj}\right) \exp\left(e\varphi_{obj}/kT_e\right) - J_{i-env} A - C\,\varphi_{obj}/\tau_R \qquad (9)$$

where φ_{obj} is set equal to an initial value φ_o from tribocharging. The φ_{obj}/τ_R term is included in the formalism and represents the dissipation of charge into the lunar regolith. τ_R is the dissipation time defined by the regolith permittivity and conductivity as ε_o/σ_R ~ 1000 s within cold PSC [*Carrier et al.*, 1991].

[39] Figure 11 shows the electrical dissipation at a location of x = 18.6 km, 20 km, and 40 km along the crater floor

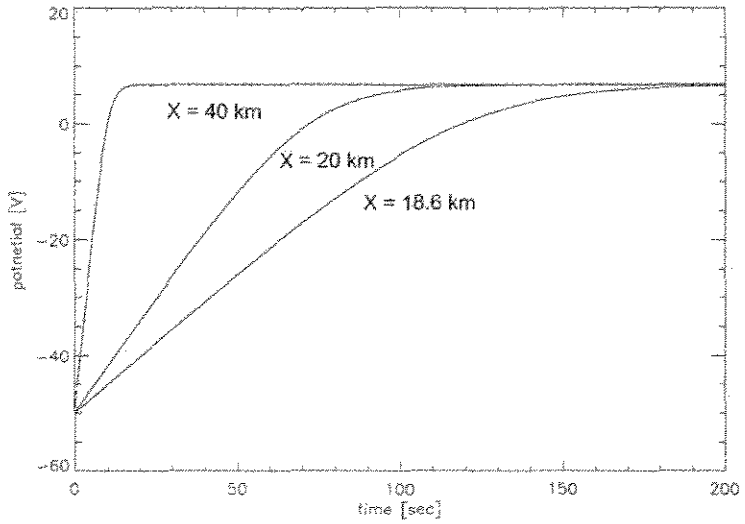

Figure 11. The electrical dissipation of an object of 1 m^2 surface area placed within Shoemaker crater at a location of x = 18.6 km (near westward wall), 20 km, and 40 km in Figure 6. The solar wind parameters are those applied to Figure 6. Table 1 provides further details on dissipation times and equilibrium values. The object is initially tribocharged to −50 V relative to the surrounding surface and has a secondary emission efficiency $\delta_{eff}^{obj} \sim 0.5$. Note that near the leeward flowing side of the crater (at x = 18.6 km), electrical dissipation of the −50 V object takes many tens of seconds due to the low levels of ambient plasma currents at levels of a few 10^{-11} A/m^2. Thus, environmental currents cannot easily remediate the excess charge buildup at such locations. Closer to the middle of the crater (x = 40 km), plasma currents are larger and thus dissipate the charge buildup faster (on time scales of seconds). The equilibrium potential is that relative to the total surface potential and is typically +6 to +45 V positive relative to the surface potential depending upon the specific value of δ_{eff}^{obj} (see Table 1).

for an object of current collecting area, A = 1 m^2. Table 1 also lists these electrical dissipation 1/e times. These values are calculated for nominal conditions like that for Figure 7a (n_{eo} = 5/cm^3, 10 eV temperature, Vsw ~ 400 km/s, a 15 m Debye length, ω_{pi} = 3000/s, and θsw = 0° directed out of the west). Note that at x = 18.6 km, for an initial tribocharge of −50 V, it takes over 100 s to return to ambient potential values defined by current balance ($d\varphi/dt = 0$). The local currents at 40 pA/m^2 are so low that there is little environmental charge to be drawn at the western edge of the crater. In contrast, further eastward of this wall, plasma flow is not as restricted, allowing more environmental current to be diverted into the crater floor via the ambipolar potential. As a consequence, dissipation times progressively decrease with distance from the leeward-facing wall (Table 1). Hence, at x = 40 km, the local currents are ~0.5 nA/m^2 and the corresponding dissipation time is on the order of 5 s. Note that these dissipation times are far slower than those in directly sunlit regions where local currents are at micro-Amp/m^2 levels and dissipation occurs on time scales of milliseconds [*Farrell et al.*, 2008b]. Also note that these times vary inversely with effective radius: an object 10 times smaller will take 10 times longer to dissipate charge. Thus, a rover wheel may take hundreds of seconds to reach equilibrium levels.

[40] The dissipation times calculated in Table 1 are for locations where ions are fully capable of flowing. However, the situation may become very complicated in locations without ions in the electron cloud where the ambipolar expansion processes are charge nonneutral [*Crow et al.*, 1975]. Consider an object roving in a region where there is an electron cloud/void of ions. Further, assume this object obtains progressively larger negative tribocharge from the very insulating regolith. As the object moves over the surface and charges negative, the overlying regolith just roved over will tribocharge to a more positive potential than that of the object. The strongly negatively charged object will repel local electron currents, but will attract objects of differing potential: like that very dust just roved over. The local dust of lower potential thus becomes the "current of last resort" to remediate the object's negative charge buildup. This effect may lead to increased dust clinging in electron cloud regions. This regolith attachment is consistent with the picture that small charged particulates become a significant current source to stem hypercharging by the object. We describe the process of dissipation in an electron cloud herein (for the first time), recognizing that modeling of such an effect is for a future effort.

7. Plasma Expansion and Its Affect on Accumulated Volatiles Within PSCs

[41] Without the inclusion of ambipolar plasma wake expansion processes, solar wind ions would simply pass over the polar crater and not easily move into the deep void regions. As indicated in Figure 1, ambipolar expansion E

Table 2. Ion Sputtering Loss Rate of Ice Within Shoemaker Crater for the Electrical Environment Shown in Figure 6 and Table 1[a]

	x (km)				
	18.6	20	30	40	50
J_i (A/m^2)	4.6×10^{-11}	7.7×10^{-11}	1.0×10^{-9}	5.4×10^{-10}	6.7×10^{-9}
n_i/n_{io}	1.1×10^{-4}	2.0×10^{-4}	3.0×10^{-3}	1.6×10^{-3}	2.0×10^{-2}
Ion Energy (keV)	1.27	1.14	0.95	0.88	0.85
Y, Yield for Ice Sputtering[b] (molecule/incident ion)	0.8	0.8	0.8	0.8	0.8
F, Ion Flux (1/m^2 s)	2.9×10^8	4.8×10^8	6.5×10^9	3.3×10^9	4.2×10^{10}
Φ = YF, Sputtering Rate(1/m^2 s)	2.3×10^8	3.8×10^8	5.2×10^9	2.6×10^9	3.3×10^{10}
Loss time for 1 μm layer of ice (kyr)	4628	2801	205	409	32

[a]Here n_i/n_{io} is the ratio of wake ions to the free-flowing solar wind density of 5/cm^3. The crater edge is x ~ 18.6 km location. Yields are for normal incidence.
[b]*Johnson* [1990, Figure 3.22b].

fields deflect the solar wind inward into the initial void regions, allowing ions to be incident or strike at the crater floor (see J_i, Table 1). Such ions may be sources of sputtering which may act to erode local volatiles (e.g., water ice) that have accumulated at the surface of the PSC.

[42] Table 2 shows the effects of ion sputtering from an icy surface on the crater floor, assuming the deflection of solar wind protons as modeled in Figure 6 and Table 1 (n_{eo} = 5/cm^3, 10 eV temperature, V_{sw} ~ 400 km/s, δ_{eff} ~ 0.3, θ_{sw} = 0°). The ice sputtering yields for H^+ of ~0.8 molecule per incident ion are from Figure 3.22b of *Johnson* [1990]. Note that sputtering loss of water is greatest in the central crater region (x = 50 km) where inflowing ion densities are relatively high (at ~2% solar wind levels).

[43] Table 2 also shows the loss rate of a polar ice layer in units of kiloyears per micron of water layer thickness. Note that in the central region, a water layer is eroding ~120 times faster than it is at the leeward edge of the crater. However, we note that the leeward edge of the crater changes position over the course of a lunation: thus the ion influx varies from small to large as the wall surface normal rotates from antisunward to sunward directed. Solar illumination will also vary at the rim of the crater as a function of lunation as well, possibly exposing the rim region to direct sunlight and more positive surface potentials (e.g., see the x = 70 km region in Figure 6). Thus, the low erosion rates along the crater wall are only realized for a fraction of each lunation.

[44] While we model the relatively large Shoemaker crater, we note that small but deep polar craters may experience the least overall ion erosion, as suggested by Table 2. For example, consider a case of a 5 km deep crater that extends only 20 km in diameter (x = 40 km position in Table 2). In this case, the water loss rate in the crater never drops below 0.4 My per micron anywhere along the crater floor, and erosion via ion sputtering will take a relatively long time. In larger craters greater than 30 km (x = 50 km position in Table 2) overall ion inflow to the floor is greater resulting in substantial ion/surface incidence which speeds up erosion.

[45] However, the situation may be different if the substrate layer is the regolith itself (e.g., SiO_2 with no overlying ice layer). In this case, the sputtering yields are low, on the order of ~0.03 molecules per incident ion for ~1 keV H^+ incidence [see *Johnson*, 1990, equation (3.15), Figure 3.16b, and Figure 3.17]. These values are about a factor of 50–100 times lower than the yield of ice. Such values suggest that any solar wind ion incident on the polar regolith will not release material but instead become mass accumulated. As such, with a nonice lunar regolith surface, ion deflection into the crater becomes a source of H^+ at the surface [*Feldman et al.*, 2001; *Crider and Vondrak*, 2003].

8. Conclusion

[46] The case is made that large-scale structures along the lunar terminator and polar regions can obstruct the solar wind (referred to herein as "solar wind orographic effects"), creating a wake region in the downstream flows. These plasma miniwakes are subject to well-known plasma ambipolar expansion processes that define the electric potential structure at the surface of leeward mountain faces and within polar shadowed craters. On the leeward sides, plasma currents are vastly reduced, and ambipolar potentials develop as electrons migrate into the shadowed regions ahead of slower, massive ions. We apply analytical models [*Crow et al.*, 1975; *Samir et al.*, 1983] (that are also consistent with simulations; *Farrell et al.* [2008a]) of the ambipolar process to define the near-surface ambipolar potentials and currents reaching the leeward side of lunar obstacles in a near-horizontal solar wind flow at the lunar polar region. These ambipolar-created currents are then used in a second calculation to derive the potential directly at the surface where all currents are balanced to equal values. We note that there are regions along the crater floor where the expansion loses neutrality (ion flow cannot reach the surface). At these locations, an electron cloud is formed. The formation of the electron cloud is also consistent with kinetic simulations of the expansion [see *Farrell et al.*, 2008a, and references therein].

[47] Within lunar craters, the surface potential can be derived in most locations. However, those locations lacking ion flow (i.e., electron cloud regions) cannot be properly balanced without the inclusion of some new downward positive/upward negative current. There are a number of possible choices for this remediative current, and one obvious (albeit nonunique) source is the current produced by lofted negatively charged dust from regions within the electron cloud. Observations from Apollo 17's surface LEAM experiment indicate that dust activity increases at terminator crossings where local orographic effects from nearby mountains are the largest. Hence, there is Apollo observational evidence that we might expect surface-ejected dust to provide the needed currents. Using LEAM results (as a starting point) we suggest that dust provides an upward negative current of $>10^{-14}$ A/m^2. Using this value, we can obtain the needed current balance – and find that the surface potentials, φ_s, can become more sharply negative within the

electron cloud regions, relative to the nominal solar wind flowing over the top of the shadowed region (see Figure 6).

[48] We suggest that lifted dust is not simply a "science curiosity" but may provide a critical role in the closure of current balance in ambipolar-created electron cloud regions. Negatively charged dust is lofted from the hypercharged surface covered by the electron cloud in an attempt to remediate the excessive charge buildup at the surface/cloud interface. The charged dust becomes the current of last resort that is expelled in an attempt to achieve current balance (attempts to reduce dQ/dt). As such, this picture of ejected/lofted dust fits naturally in the overall picture of the electrical environment within polar shadowed craters and behind obstructing mountains. We would thus predict that LEAM's "dusty sleet" should be anticipated in the polar environment that is essentially in a perpetual terminator. Clearly, some sort of precursor validating observation is required to confirm this prediction, but there is certainly an analog with the equatorial Taurus-Littrow valley where energetic dust at terminator crossings was reported. We note that there may be other ways to obtain current balance (increased secondary electron emission, field emissions, etc.) and these need to be investigated in the future as well.

[49] Given the overall electrical environment, we can then consider the electrical fate of objects placed within the PSCs. We find that stationary objects tend to charge positive relative to the surface (still negative relative to the overflowing solar wind), with the largest differential charging occurring with objects that have a secondary electron coefficient that has the greatest difference from the lunar regolith. If the object has secondary electron emission similar to the lunar regolith, the differential potential between the object and lunar surface is reduced almost to zero.

[50] Of concern is electrical dissipation of any tribocharge buildup from a moving object, since both lunar surface currents and plasma currents are reduced in PSCs. It was found that dissipation time scales can become very large near the leeward face of PSCs with equilibrium times achieved in 100 s of seconds in regions of low ion currents (leeward crater walls). Within the electron cloud, we again demonstrate that plasma currents will likely have difficulty obtaining balance at the object. We suggest that the recently tribocharged regolith that has just been churned by the object then act as the remediation current of "last resort." However, this current may still not dissipate charge as fast as bleeding the object charge directly into the low conductivity ground (i.e., directly into the insulating regolith). As such, we expect very slow dissipation times (~1000 s) within electron cloud regions of PSCs. Certainly, if any human object is roving in the leeward edges of the craters, special care must be made for avoidance of electrostatic discharge hazards.

[51] The modeling, based on previous analytical [*Crow et al.*, 1975; *Samir et al.*, 1983; *Manka*, 1973; *Stubbs et al.*, 2006] and simulation [*Farrell et al.*, 1998; *Birch and Chapman*, 2001a, 2001b; *Farrell et al.*, 2008a] studies, applies ambipolar and wake expansion in the vertical plane. As an example, for a mountain we consider the expansion as a function of vertical dimension. However, we do not consider expansion about the edges of a feature (like a mountain), in a horizontal plane parallel to the surface. A 3-D PIC code could model the multidimensional system and should be consider for future work. Such a model may also include plasma transport from implanted ions on the windward side and their transport over the topographic feature into the expansion region. This "ion leakage" might also be a current to remediate large surface potential regions. We do not model such effects herein. We also assume a Maxwellian plasma distribution describes the ambient solar wind and expansion region and future efforts could incorporate a kappa distribution [*Halekas et al.*, 2005]. Ideally, a multidimensional kinetic simulation can be used to consider expansion about a complex object. However, the results here provide a first-order estimate of surface potentials.

[52] We also assume that the plasma is flowing unconstrained by local magnetic fields: that there are no surface magnetic fields in the PSC region. Such fields (as yet to be identified) will alter plasma geometries and currents, with the result in most locations being to further reduce the currents reaching the surface [*Reiff*, 1976]. As an example, as solar wind electrons move close to the surface and into increasingly converging magnetic field geometries, electrons of large pitch angle are reflected at the mirror points and thus never reach the surface. As such, there would be an additional electron and ion retardation factor to equations (5) and (6), further increasing dissipation times via plasma return currents.

[53] We disconnect the solution of the ambipolar potential, φ_A, to that of the surface potential, φ_s, and this is allowable due to the development of the Debye sheath at the surface. The sheath plasma is specifically formed to cancel the electrical forces from the surface and as such the surface charge does not affect the formation of the ambipolar expansion (except at regions where $\Delta z < \lambda_D$). This expansion proceeds with minimal influence from the surface below. As such, the two processes can be calculated independently and solutions merged piecemeal. This situation is unlike an infinitely extended surface in free space, where any surface charge alters potentials out to infinity. In the lunar case, the surface is shielded by a conductive (plasma) medium that polarizes charge near the surface (the sheath charge) to exactly cancel the surface charge beyond a few Debye lengths. The potential from this surface goes to zero at infinity.

[54] Secondary electrons have been lumped into a bulk parameter, δ_{eff}, but are of special interest. Specifically, they are released from the surface in low concentrations: the densities are low enough ($n_{sec} \sim \delta_{eff}\, n_{eo} \exp(e\varphi_A/kT_e)$ for φ_A at the surface) that they should not significantly modify the ambipolar potential structure at altitudes above the surface. We assume that this is the case, but note that even weak beams can affect local potentials in nonlinear ways and such should be examined in more detail. The beams are accelerated through the sheath and ambipolar potentials to form well-defined beams at very high altitudes, like those detected by Lunar Prospector [*Halekas et al.*, 2002, 2009a]. As such, these emissions become an on-orbit remote sensing tool to determine the underlying near-surface potentials.

[55] An assertion of this work is that dust is most likely and easily lofted from crater floors in regions where the surface potential is the largest. Hence, a simple way to sample resources within the lunar craters is to perform dust collection from orbit – and let the crater surface electrical effects move material from the surface to orbiting altitude. In essence, we let the lunar environment provide the "heavy

lifting" of material so that a sampling system does not have to perform a difficult landing and return liftoff within the cold, electrically complicated crater.

[56] The situation may also be true at a base located near/above the PSC. Because of electrical repulsion effects, LEAM-like dust containing internal crater resources (i.e., water) may be ejected out of the crater floor and onto the surrounding surface. This effect will maximize when the solar wind is flowing in the direction over the crater and the lunar base is downstream. In this case, the surface normal of the leeward edge of the crater points toward the lunar base – directing material in the direction of the base itself. As such, explorers may not have to go into the cold craters to determine if resources are present: they may simply "pop out" of the crater to them. The question is if the amount being ejected is enough to be of any real value to a landed exploration team. A precursor environmental mission would answer this question. We thus conclude that the environment has significant electrical variability: but this same electrical variability may be used to the advantage of any exploration team.

[57] **Acknowledgments.** This work was initially enabled by support from NASA's Exploration Technology Development Program (ETDP) and GSFC Internal Research and Development (IRAD) program. Recent augmentation of support into FY09 is provided via the NASA's LASER program, LRO Participating Science program, and NASA's Lunar Science Institute, awards which we gratefully acknowledge. B.A. Campbell and J.L. Margot are both acknowledge for directing us to the locations for access to the Goldstone Radar data.

References

Berg, O. E., and D. Perkins (1979), Response of lunar ejecta and meteorites experiment (LEAM) to electrostatically charged lunar dust, *Space Sci. Instrum.*, *4*, 329.

Berg, O. E., et al. (1976), Lunar soil movement registered by the Apollo 17 cosmic dust experiment, in *Interplanetary Dust and Zodiacal Light*, edited by H. Elsasser et al., pp. 233–237, Springer, Berlin.

Birch, P. C., and S. C. Chapman (2001a), Particle-in-cell simulations of the lunar wake with high phase space resolution, *Geophys. Res. Lett.*, *28*, 219, doi:10.1029/2000GL011958.

Birch, P. C., and S. C. Chapman (2001b), Detailed structure and dynamics in particle-in-cell simulations of the lunar wake, *Phys. Plasmas*, *8*, 4551, doi:10.1063/1.1398570.

Carrier, W. D., G. R. Olhoeft, and W. Mendell (1991), Physical properties of the lunar surface, in *The Lunar Sourcebook*, edited by G. H. Heiken et al., pp. 475–594, Cambridge Univ. Press, Cambridge, U. K.

Crider, D. H., and R. R. Vondrak (2003), Space weather effects on lunar cold trap deposits, *J. Geophys. Res.*, *108*(E7), 5079, doi:10.1029/2002JE002030.

Crow, J. E., P. L. Auer, and J. E. Allen (1975), The expansion of plasma into a vacuum, *J. Plasma Phys.*, *14*, 65, doi:10.1017/S0022377800025538.

Desch, S. J., and J. N. Cuzzi (2000), The generation of lightning in the solar nebula, *Icarus*, *143*, 87, doi:10.1006/icar.1999.6245.

Farrell, W. M., M. L. Kaiser, J. T. Steinberg, and S. D. Bale (1998), A simple simulation of a plasma void: Applications to wind observations of the lunar wake, *J. Geophys. Res.*, *103*, 23,653, doi:10.1029/97JA03717.

Farrell, W. M., T. J. Stubbs, R. R. Vondrak, G. T. Delory, and J. S. Halekas (2007), Complex electric fields near the lunar terminator: The nearsurface wake and accelerated dust, *Geophys. Res. Lett.*, *34*, L14201, doi:10.1029/2007GL029312.

Farrell, W. M., T. J. Stubbs, J. S. Halekas, G. T. Delory, M. R. Collier, R. R. Vondrak, and R. P. Lin (2008a), Loss of solar wind plasma neutrality and affect on surface potentials near the lunar terminator and shadowed polar regions, *Geophys. Res. Lett.*, *35*, L05105, doi:10.1029/2007GL032653.

Farrell, W. M., T. J. Stubbs, G. T. Delory, R. R. Vondrak, M. R. Collier, J. S. Halekas, and R. P. Lin (2008b), Concerning the dissipation of electrically charged objects in the shadowed lunar polar regions, *Geophys. Res. Lett.*, *35*, L19104, doi:10.1029/2008GL034785.

Feldman, W. C., et al. (2001), Evidence of water-ice near the lunar poles, *J. Geophys. Res.*, *106*, 23,231, doi:10.1029/2000JE001444.

Halekas, J. S., et al. (2002), Evidence for negative surface charging of the lunar surface in shadow, *Geophys. Res. Lett.*, *29*(10), 1435, doi:10.1029/2001GL014428.

Halekas, J. S., S. D. Bale, D. L. Mitchell, and R. P. Lin (2005), Electrons and magnetic fields in the lunar plasma wake, *J. Geophys. Res.*, *110*, A07222, doi:10.1029/2004JA010991.

Halekas, J. S., G. T. Delory, D. A. Brain, R. P. Lin, M. O. Fillingim, C. O. Lee, R. A. Mewaldt, T. J. Stubbs, W. M. Farrell, and M. K. Hudson (2007), Extreme lunar surface charging during solar energetic particle events, *Geophys. Res. Lett.*, *34*, L02111, doi:10.1029/2006GL028517.

Halekas, J. S., et al. (2009a), Lunar Prospector measurements of secondary electron emission from lunar regolith, *Planet. Space Sci.*, *57*, 78, doi:10.1016/j.pss.2008.11.009.

Halekas, J. S., et al. (2009b), Lunar surface charging during solar energetic particle events: Measurement and prediction, *J. Geophys. Res.*, *114*, A05110, doi:10.1029/2009JA014113.

Johnson, R. E. (1990), *Energetic Charged Particle Interactions With Atmospheres and Surface*, Spinger, New York.

Manka, R. H. (1973), Plasma and potential at the lunar surface, in *Photon and Particle Interactions With Surfaces in Space*, edited by R. J. L. Grard, pp. 347–361, Reidel, Dordrecht, Netherlands.

Margot, J. L., et al. (1999), Interferometry: A survey of cold trap locations topography of the lunar poles from radar, *Science*, *284*, 1658, doi:10.1126/science.284.5420.1658.

Ogilvie, K. W., J. T. Steinberg, R. J. Fitzenreiter, C. J. Owen, A. J. Lazarus, W. M. Farrell, and R. B. Torbert (1996), Observations of the lunar plasma wake from the wind spacecraft on December 27, 1994, *Geophys. Res. Lett.*, *23*, 1255, doi:10.1029/96GL01069.

Reiff, P. H. (1976), Magnetic shadowing of charged particles by an extended surface, *J. Geophys. Res.*, *81*, 3423, doi:10.1029/JA081i019p03423.

Samir, U., K. H. Wright Jr., and N. H. Stone (1983), The expansion of a plasma into a vacuum: Basin phenomena and processes and applications to space plasma physics, *Rev. Geophys.*, *21*, 1631, doi:10.1029/RG021i007p01631.

Singh, N., K. H. Wright Jr., N. H. Stone, U. Samir, and K. S. Hwang (1989), On the interpretation of measured ions streams in the wake of the shuttle orbiter in terms of plasma expansion processes, *J. Geophys. Res.*, *94*, 12,075, doi:10.1029/JA094iA09p12075.

Stubbs, T. J., R. R. Vondrak, and W. M. Farrell (2006), A dynamic fountain model for lunar dust, *Adv. Space Res.*, *37*, 59, doi:10.1016/j.asr.2005.04.048.

Vondrak, R. R., and D. H. Crider (2003), Ice at the lunar poles, *Am. Sci.*, *91*, 322.

M. R. Collier, W. M. Farrell, R. M. Killen, T. J. Stubbs, and R. R. Vondrak, NASA Goddard Space Flight Center, 8463 Greenbelt Rd., Greenbelt, MD 20770, USA. (william.farrell@gsfc.nasa.gov)

G. T. Delory and J. S. Halekas, NASA Lunar Science Institute, NASA Ames Research Center, Moffett Field, CA 94035, USA.